Optical and Quantum Electronics (2020) 52:245
https://doi.org/10.1007/s11082-020-02362-0

Dependence of mobility and charge injection on active layer thickness of bulk heterojunction organic solar cells: PCBM:P3HT

Lordwell Jhamba[1,2] · Daniel Wamwangi[1] · Zivayi Chiguvare[3]

Received: 30 November 2019 / Accepted: 15 April 2020 / Published online: 28 April 2020

Abstract
The asymmetric behavior in the dark current of any solar cell is essential for decoupling recombination and charge extraction for efficient charge collection. Therefore current density dependence on applied voltage can be used to investigate the complex interplay between bulk charge transport, interface exchange effects and recombination mechanisms. In the present work, we investigate from dark current–density [J(V)] of bulk heterojunction solar cells, the dependence of mobility and charge injection mechanisms on different blend layer thicknesses. The active layer thickness has been established through varying the spin-coating speeds between 1000, 2000, 3000 and 4000 revolutions per minute (rpm) and confirmed by a dektak surface profilometer. The carrier mobility (μ) as a factor limiting the efficiency of organic solar cells was investigated from dark space charge limited current and trap free space charge limited current conduction mechanisms to distinguish between charge extraction and recombination. This approach allows the determination of the effects of threshold field through variation of the active layer thickness (ALT) on the potential barrier height (ϕ_B) at the electrode contacts. Low values of charge carrier mobilities (10^{-6} cm^2 V^{-1} s^{-1}) in the trap free space charge limited current conduction region have been correlated to the Langevin recombination constants. In the ohmic region, the highest dark carrier mobility corresponded to the 77.1 nm ALT. Further we observe a shift in the transition voltage at the inflection point of J–V curves with increasing film thickness in the forward bias.

Keywords Dark space charge limited current · Langevin recombination · Saturation current · Field emission

Electronic supplementary material The online version of this article (https://doi.org/10.1007/s11082-020-02362-0) contains supplementary material, which is available to authorized users.

✉ Daniel Wamwangi
daniel.wamwangi@wits.ac.za

Extended author information available on the last page of the article

1 Introduction

The lure of organic solar cells (OSCs) is increasing due to their unique opto-electrical properties. The ability to tune photoabsoption to match the photon flux of the solar emission spectrum as well as their low cost processibility have recently led to high photoconversion efficiency in the excess of 13%. More recently the use of non fullerene polymers has further steered research interest in organic photovoltaic due to the attainment of high efficiencies with reasonable device stability. This has paved the way for the potential application as flexible, low weight and scalable large area devices in consumer electronics (Shieh et al. 2010; Schilinsky et al., 2002; Padinger et al. 2003; Chirvase et al. 2004; Sirringhaus et al. 1999; Islam et al. 2013; Kadem et al. 2016; Huang et al. 2015; Peters et al. 2011). Moreover their light weight is convenient in off grid power production for application in such gadgets as one child laptop (Wehenkel 2012; https://one.laptop.org/), or solar lamps (Krebs et al. 2010). Although recent research improvements in bulk heterojunction (BHJ) solar cells have produced significant increase in the power conversion efficiencies surpassing the 10% limit (Peters et al. 2011; Dimitrov et al. 2016; Mesbahus et al. 2016; Che et al. 2018), their efficiencies are still not high enough to be commercially viable (Scharber et al. 2006; Dennler et al. 2008; Nam et al. 2010). However, prerequisite to overcoming the hindrances is a thorough understanding of device physics, charge transport and recombination mechanisms in the layer stack of OPV cells. Such understanding can be enhanced through knowledge of the dark characteristics of OPVs.

Dark characteristics of solar cells enable in the determination of the fundamental parameters that determine device performance. In some instances while operating under illumination the effect of electrode induced charge recombination on the photocurrent can be elucidated. Therefore, the J–V analyses under dark conditions for varied active layer thickness provide insights on the nature of mobility limited recombination losses and also on the electrode induced charge carriers which degrade the fill factor and thus impact on the device's power conversion efficiency (Qi and Wang 2013). These parameter values are dependent on the active layer thickness (ALT) of the device, because it (ALT) affects light absorption by the active layer, mobility and morphologically based competing processes in the active layer. Some of the processes pit migration of charge carriers to electrodes against recombinations in the active layer. Therefore, it is imperative to establish the optimal active layer thickness that allows for optical absorption, low series and high shunt resistances.

The dark current density–voltage characteristics of different ALT devices are studied for determination of the interplay between bulk transport and interfacial exchange effects that might contribute to recombination. This is carried out by analysis of the dark space charge limited current (SCLC) conduction and charge injection mechanisms at electrical contacts in the dark, with focus on the potential barrier height (φ_B) dependence on the active layer thickness (ALT) based on Fowler–Nordheim (FN) quantum mechanical tunneling (field emission) and Richardson-Schottky (RS) thermionic emission formulations.

2 Theoretical framework of charge injection and extraction mechanisms

In organic solar cells, the charge carrier mobility μ simultaneously controls both the carrier extraction and recombination losses (Mandoc et al. 2007; Shaheen et al. 2001; Kao et al. 1983; Koetse et al. 2006; Langevin 1903). Thus for effective charge transport, a balance of charge carrier extraction and recombination is prescribed. More recently, the competition factor has exhibited dependence on the generation rate and carrier mobility from the thickness and electric field measurements by impedance spectroscopy (Kirchartz et al. 2012; Heiber et al. 2018). Despite this determination, the effect of the built-in field and the injection of minority charge carriers for devices with varying active layer thickness is insufficiently studied. Therefore optimal charge carrier mobility to enhance the photoconversion efficiency is requisite especially in instances that determine the recombination of minority carriers at the interface of the active layer and the electrodes. Recombination losses under low mobilities stifle the solar cell performance, whereas the efficient extraction at high mobilities leads to reduction in the open circuit voltage due to the formation of the surface dipoles at the electrodes (Mandoc et al. 2007).

The charge injection mechanisms at metal/active layer junctions are described by Fowler–Nordheim (FN) and Richardson-Schottky (RS) formalisms. Fowler–Nordheim field emission model assumes quantum tunneling of carriers through a triangular potential barrier into unbound continuum states to yield current density J of the form (Sze 1981);

$$J = AF^2 \exp\left(-\frac{8\pi\sqrt{2m^*}\,\varphi_B^{3/2}}{3hqF}\right) \tag{1}$$

where m^* is the effective mass of the charge carrier, F is the applied electric field (equivalently given by $F = \frac{V}{d}$, in which d is the active layer thickness), A (in A/V^2) is a rate coefficient that contains a tunneling prefactor and rate of current back-flow, h is the Planck constant equal to 6.626×10^{-34} m^{2}kg/s and q is the electronic charge.

Alternatively, the Richardson–Schottky (RS) thermionic emission model attributes the resultant current to electrons with energies in excess of the conduction band energy at the metal-polymer junction. Therefore the lowering effect of the image force on the potential height leads to current density in the form; (Chiguvare 2005; Kao and Hwang 1981; Das et al. 2002; Henisch 1984; Braun 2003)

$$J = A^*T^2 \exp\left(\frac{-\varphi_B}{k_BT}\right) \exp\left[\left(\frac{q^3V}{4\pi\varepsilon_0\varepsilon_r d}\right)^{\frac{1}{2}}/k_BT\right] \tag{2}$$

where ϕ_B, d, ε_0 and ε_r are the interface potential barrier height, active film thickness, permittivity of free space and relative permittivity (optical dielectric constant) respectively; k_B is Boltzmann's constant, q is the elementary (electronic) charge, T is the thermodynamic temperature, V is the applied (bias)voltage (which is positive for forward bias and negative for reverse bias) and A^* is the Richardson-Schottky constant (Chiguvare 2005; Henisch 1984).

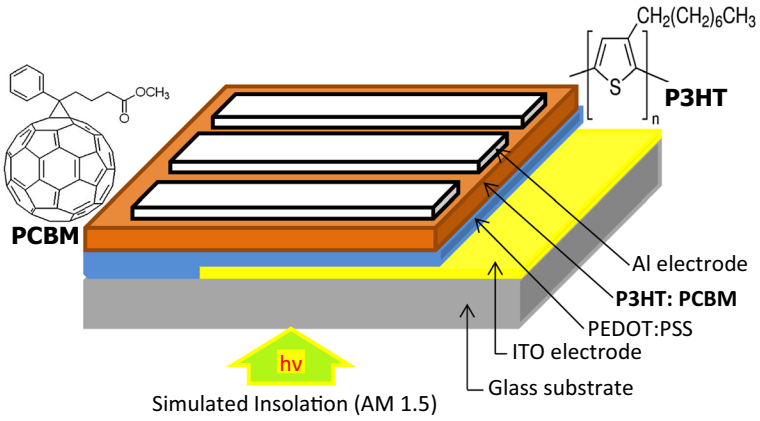

Fig. 1 Bulk heterojunction solar cells alongside the structural formulae of components of the active layer (P3HT and PCBM)

3 Materials and methodologies

All bulk heterojunction solar cells were fabricated using the device architecture shown in Fig. 1. In total 36 devices of cross-sectional area $(7 \pm 1)\text{mm}^2$ were analysed for charge injection, transport and extraction.

Device fabrication was carried out by firstly spin coating PEDOT:PSS solution on patterned and thoroughly cleaned ITO coated glass substrates at a constant speed of 2000 rpm for 60 s. A bake out was carried out at 120 °C for 15 min to remove the adsorbed water and enhance the stability of the PEDOT:PSS-active layer interface (Liao et al. 2010; Kandjani et al. 2015).

The active blend was formed by dissolving of 7.5 mg of regioregular head-to-tail poly(3-hexylthiophene-2,5-diyl) (P3HT), (electron donor, purchased from Sigma Aldrich) and 7.5 mg of [6,6]-phenyl C_{61} butyric acid methyl ester (PCBM), (the electron acceptor) separately in 0.5 ml chlorobenzene. To ensure homogenous dissolution, the P3HT and PCBM solutions were each magnetically stirred for 3 h at room temperature.

The active blend solution of P3HT and PCBM was then made by mixing the two solutions (in the matrix P3HT:PCBM = 1:1 by mass and concentration 15 mg/ml) and subjecting the mix to magnetic stirring for a further 2 h in ambient. To obtain different active layer thicknesses (ALTs), the active mix was cast on each of the four 1.25 cm × 1.25 cm glass/ITO/PEDOT:PSS substrate bases at different spin-coat speeds. The spin-coat speeds used were 1000, 2000, 3000 and 4000 rpms for 60 s. All spin coatings were done at room temperature and standard conditions. The resultant film thickness was measured by Dektak

Table 1 Spin-coat speeds and corresponding active layer thicknesses

Sample/device name	Spin-coating speed (rpm)	Active layer thickness (nm)
S_1	1000	84.5 ± 2.0
S_2	2000	77.1 ± 1.5
S_3	3000	69.4 ± 1.1
S_4	4000	61.5 ± 0.8

surface profilometer as presented in Table 1. The spin coated device was metallized by thermal evaporation of Al top electrode (~ 100 nm) under high vacuum; 1.5×10^{-6} mbar.

4 Results and discussion

4.1 Dark J(V) characteristics of different ALT devices

The rectification characteristics of each device in the dark is presented in the supplementary material of Fig. S1. The presence of five regions (FI, FII, FIII, RI, RII and RIII) exhibiting varied charge transport characteristics are evident. These regions approximate boundaries of numerous competing recombination and charge extraction processes within the active layer and interfaces. In each of the identified regions, the dark current density, J (or J_{dark}), at a given voltage increases for the different thicknesses.These results are attributed to the modifications of the charge carrier injection barriers as well as mobility. The changes in the nanomorphology and domain sizes for different thicknesses are however less likely as posited in (Nam et al. 2010). The variation in the rectification factors at 1.00 V is indicative of varying potential energy barriers at the metal-active layer interfaces of the devices under reverse bias as will be demonstrated by the inflection point of the J–V curves in the F–N field emission model.

It is noted that the optimum J_{dark} values in the identified forward and reverse bias regions prevail more in the 77.1 nm active layer thickness devices. The effect of the parasitic resistances on the dark and 100 mW/cm^2 illumination curves for the optimal thickness (77.1 nm) is presented in Fig. 2a. It is evident that the photovoltaic action is limited by R_s and R_{sh}.

According to Eq. (S1), the J(V) curve of the solar cell is divided into three regions, both in the dark and under illumination (Servaites et al. 2011; Stevens et al. 2009). The equivalent regions for the different thicknesses in semi-logarithmic representation under dark are shown in Fig. 2b. At low positive voltages (corresponding to Region I in Fig. 2a, b) the J(V) curves are straight lines with slopes determined by the $1/R_{sh}$. If R_{sh} decreases, the slope of the J(V) curve increases.

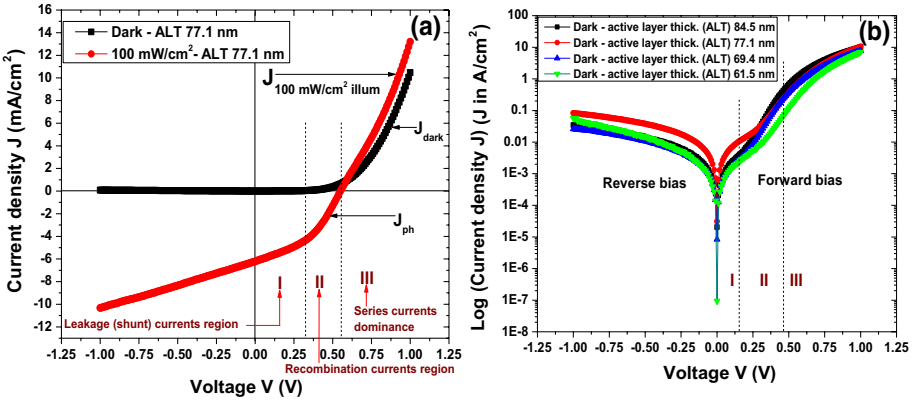

Fig. 2 **a** Typical J versus V plot for the ALT 77.1 nm device under dark and simulated 100mW/cm^2 , **b** Regions of merit for the different ALTs in semi-logarithmic representation

This makes the profile of the J(V) curve in the vicinity of J_{sc} to be less parallel to the x-axis, thus reducing the squareness, hence the fill factor and efficiency of the device. The dependence of the J(V) curve and the fill factor conforms to results by Bartesaghi et al. (2015). At intermediate positive voltages corresponding to Region II, the J(V) curves for the different thicknesses are exponential dependence in J(V). At high voltages, corresponding to Region III, the J(V) curve is linear straight line, with the slope controlled by $1/Rs$ (where $1/R_s$ is equal to dJ/dV).

4.2 Space charge limited conduction (SCLC) for different active layer thickness devices: dark characteristics

The bulk transport mechanisms in the OPV devices have been investigated through analysis of the space charge limited conduction (SCLC) processes for charge transport. In this regard, the dark J(V) characteristics of Fig. 3, are plotted in double logarithmic scale under forward bias for the different active layer thicknesses. The curves subscribe to a power law dependence of the proportionality form $J \propto V^m$ (that is, $J = cV^m \Rightarrow Log\, J = m\, Log\, V + Log\, c$), where m is the gradient and c is a constant. Three regions of bulk transport (electrical) behaviour namely I, II and III can be identified in Fig. 3. Region I is the low voltage region, located between 0 and approximately 0.18 V for the devices formed of active layer thicknesses 61.5 nm, 69.4 nm and 84.5 nm. The device with an active layer thickness (ALT) of 77.1 nm exhibits an extension of the region (that is, region I) to approximately 0.24 V. This is the region corresponding to i→e for the 77.1 nm ALT in Fig. 3.

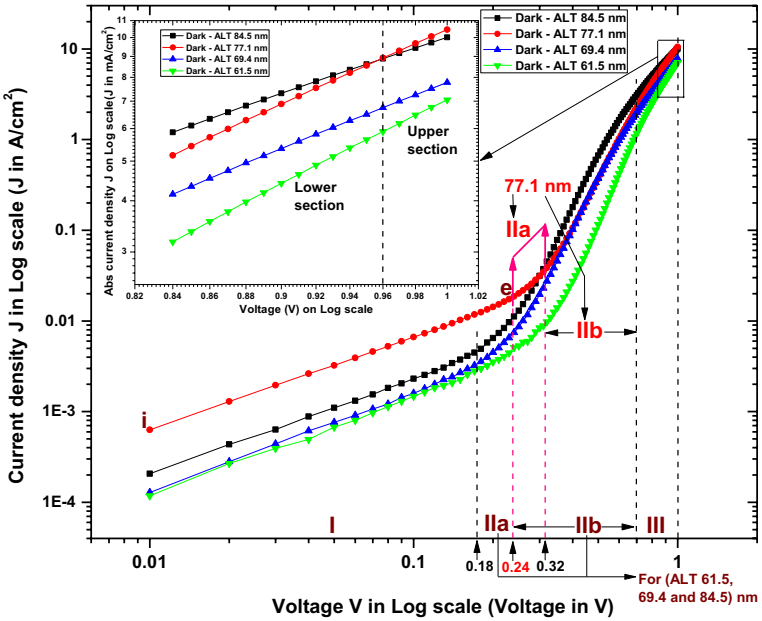

Fig. 3 Dark J(V) characteristics in double logarithmic (J–V) scale representation for ITO/PEDOT:PSS/P3HT:PCBM/Al solar cells with different 1:1 P3HT:PCBM active layer thicknesses

The slope for each layer thickness in region I is determined to m = 1.3, implying that charge transport is Ohmic (Kadem et al. 2015, 2016; Bässler 1993).

The extension of the ohmic characteristic for the 77.1 nm ALT device suggests a relatively more improved morphology as corroborated by the highest values of photocurrent density (Jsc ≅ 7.5 mA/cm^2).

In region II, two sub-regions, IIa and IIb are identified. Sub-region IIa lies between ~ 0.18 and ~ 0.24 V for the 61.5, 69.4 and 84.5 nm active film thick devices and between ~ 0.24 and ~ 0.32 V for the 77.1 nm based device. The generally higher gradients (steepnesses) of curves in region IIa when compared to those of region I show a non-ohmic nature of region IIa. In this region, the gradients on average take $m = 2.1 \pm 0.2$ and the charge transport is thus attributed to trap-controlled SCLC with traps located at a single energy level inside the band gap (Kadem et al. 2016; Gunduz et al. 2012) according to the expression

$$J = \frac{9}{8}\varepsilon_r \varepsilon_0 \theta \mu \frac{V^2}{d^3} \tag{3}$$

where $\varepsilon_r = 3.5$ is the dielectric constant (or relative permittivity) of the active blend (Kadem et al. 2016), ε_0 is the permittivity of free space = 8.854×10^{-12} Fm^{-1}, θ is the trap limiting factor (El-Nahass et al. 2007). Region IIb corresponds to the region between the voltages ~ 0.24 V and ~ 0.70 V for the 61.5, 69.4 and 84.5 nm active film thick devices and between ~ 0.32 and ~ 0.70 V for the 77.1 nm ALT device. In this region, the gradients for the differently thickened active layer devices become so highly steep that the respective m values take to the tune of the order of 10 – 13. The J(V) characteristics in this region are associated with the filling of traps (or trap filling limit) (Kadem et al. 2016). All the four ALTs show the presence of traps.

Interestingly, the curvature of the J(V) curve in the region of applied voltage between 0.7 – 1.0 V exhibits a quadratic profile indicative that almost all the traps have been filled and therefore marks the onset of trap-free space charge limited conductivity (TFSCLC). In trap-filled SCLC, the current density associated with each ALT increases quadratically with increasing applied voltage (Kadem et al. 2016; Gunduz et al. 2012) (thus, in conformity with the exhibited bowing of Fig. 3 J–V curves at higher applied voltages) because there will be no current shunting (a loss mechanism) into traps. Minimal losses if still evident would then be due to other competing mechanisms. The J–V dependence in the TFSCLC region (III) is described by Child's law (Kadem et al. 2016; Apaydin et al. 2013)

$$J = \frac{9}{8}\varepsilon \varepsilon_0 \mu \frac{V^2}{d^3}, \tag{4}$$

with $m = 2$ when strictly TFSCLC, otherwise m can take values in the range 2–3 for the rest of region III. Bulk transport conforms to Child's law when the injected charge carriers from the electrodes numerically surpass the thermally generated carriers and all traps are filled (Kadem et al. 2016; Gunduz et al. 2012). Charge carrier mobilities (μ values) are therefore field dependent. However, the role of morphology on the built-in field of the active layer cannot be neglected. In determining the charge mobility μ in the active layer, it is therefore necessary to first of all establish the region of location of the charge whose mobility is being sought. This was done through plotting log J vs log V corresponding to the section under study and determining the slope (gradient) of the resultant curve. Alternatively, by using Ohm's law to the J *vs* $\frac{V}{d}$ plot yields the mobility of the carriers in the region of interest.

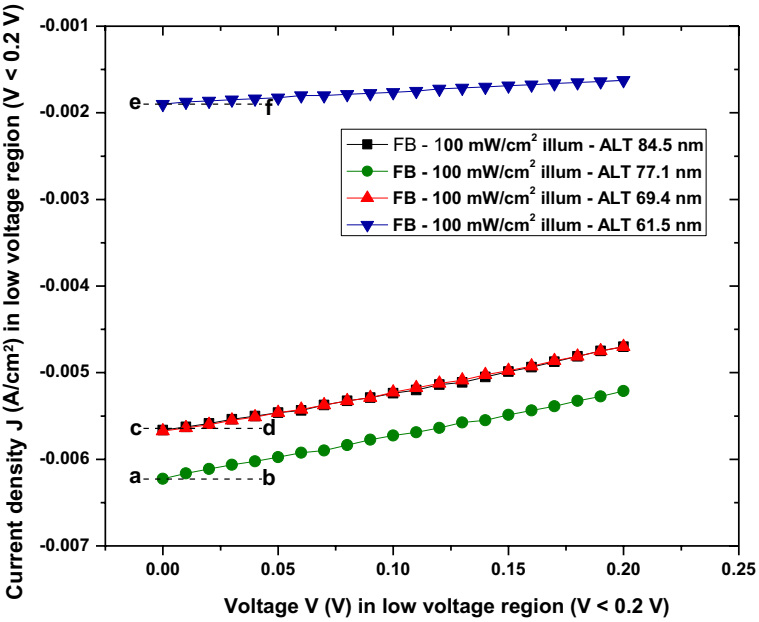

Fig. 4 J–V/d in low voltage ohmic region for the differently thickened active film devices

To this end we have plotted $J\ vs\ \frac{V}{d}$ in the ohmic region for our different active layer thickness devices as shown in Fig. 4.

Based on the visual difference in the slopes of the plots to horizontal lines (ab, cd and ef) and the exhibited corresponding current density magnitudes, we surmise that the highest (ohmic region) mobility is associated with the 77.1 nm active layer thick device (which shows the highest slope) and the lowest is ascribed to the 61.5 nm ALT, which is the thinnest.

This is also observed in the slope of log J vs log V for the TFSCLC region (that is, region III) of Fig. S2.

Based on Eq. (4) and using the identified data, we plotted $J\ versus\ \frac{V^2}{d^3}$ for each active layer thickness as shown in Fig. 5. The slope of each of the $J\ versus\ \frac{V^2}{d^3}$ curves was obtained as $\frac{9}{8}\varepsilon\varepsilon_0\mu$ and used simultaneously with Eq. (4) to determine the associated mobility μ in the form

$$\mu_{in\ the\ TFSCLC\ region)} = \frac{8}{9} \times \frac{1}{\varepsilon\varepsilon_0} \times slope \tag{5}$$

where the relative permittivity ε_r for P3HT:PCBM has been estimated to be ~ 3.5 (Kadem et al. 2015) and $\varepsilon_0 = 8.854 \times 10^{-12} Fm^{-1}$.

The values of dark charge carrier mobilities in the different active layer thicknesses corresponding to the upper section of region III, the TFSCLC region are summarized in Table 2.

Although the obtained charge carrier mobilities are in conformity with literature (Shieh et al. 2010; Kadem et al. 2016; Koster et al. 2006; Blakesley et al. 2014), they are very low in comparison with optimal mobilities of about 10^{-3} to 10^{-2} m^2/Vs (Shieh et al. 2010;

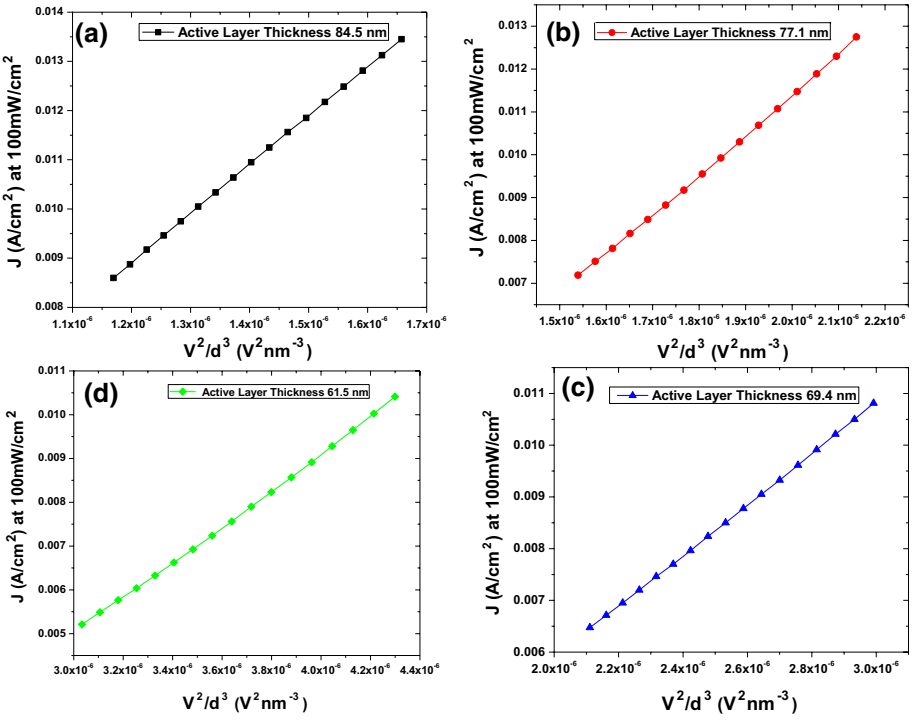

Fig. 5 *J versus* $\frac{V^2}{d^3}$ curves for upper section in TFSCLC region (III) for different ALTs

Table 2 Approximate values of charge carrier mobilities in the different active layer thicknesses for the upper section of the trap free space charge limited current (TFSCLC) region

Active layer thickness (ALT) / nm ±0.1	~(Dark) Charge carrier mobility μ (cm^2V^{-1} s^{-1}) in TFSCLC region $\pm 0.005\times10^{-6}$	Langevin recombination constant γ (cm^3s^{-1}) $\pm 0.005\times10^{-15}$
61.5	1.263×10^{-6}	6.529×10^{-15}
69.4	1.481×10^{-6}	7.656×10^{-15}
77.1	2.463×10^{-6}	1.273×10^{-14}
84.5	2.317×10^{-6}	1.198×10^{-14}

Koster et al. 2006). Overall, the charge carrier mobility values increase with increasing film thickness up to 77.1 nm ALT. Thereafter, the mobility saturates with further increase in film thickness. The minimum mobility is shown to be in the 61.5 nm ALT. This could possibly be related to the nature of the interconnected network. However, this is not validated by the J(V) characteristics under 1 Sun.

Langevin recombination is the major factor limiting the efficiency in organic solar cells (Shieh et al. 2010; Koster et al. 2006; Blakesley et al. 2014). Since recombination is mobility dependent (Shieh et al. 2010; Koster et al. 2006), the effect of charge carrier mobility on the

efficiency of OSC therefore creeps in through recombination (Shieh et al. 2010; Koster et al. 2006). Shieh et al. 2010 showed that near the short circuit condition, the photo-carrier recombination in the organic active layer decreases as the mobility increases. Here we demonstrate that in the vicinity of the open circuit condition, the dark recombination increases with mobility. For an optimal mobility (about 10^{-2} cm^2/Vs) which yields the highest power conversion efficiency, the two opposite effects need to equilibrate (Shieh et al. 2010). Although it seems well established that solar cells with Schottky barrier between the semiconductor and the metal do not experience dark carrier recombination, we confined our dark recombination study to the TFSCLC region (Shieh et al. 2010; Mandoc et al. 2007; Koster et al. 2005, 2006; Blakesley et al. 2014; Heiber et al. 2018). The Langevin recombination constant γ used in determining the recombination rate *R*, is given from (Koster et al. 2006) as

$$R = \gamma \left(np - n_{\text{int}} p_{\text{int}} \right) \tag{6}$$

where $n(p)$ is the free electron (hole) density, $n_{\text{int}}p_{\text{int}}$ is intrinsic electron (hole) density. Recombination increases in low mobility limit due to carrier accumulation inside the bulk (Shieh et al. 2010; Mandoc et al. 2007; Koster et al. 2006; Blakesley et al. 2014; Koster et al. 2005; Deibel et al. 2008; Kirchartz et al. 2009). Since our mobilities lie in the low range (less than 10^{-4} cm^2 V^{-1} s^{-1}), we determined the associated Langevin recombination constants (shown in Table 2), partly to ascertain carrier recombination dependence on the ALT dependent mobilities and for comparative use in determining whether the found mobilities are hole or electron mobilities, because our devices were bipolar devices. In calculating the Langevin recombination constant γ, we used approximation (7), due to (Koster et al. 2006), which is:

$$\gamma = \frac{q}{\varepsilon} \min \left(\mu_h , \mu_e \right) \tag{7}$$

where, μ_h and μ_e are the hole and electron mobilities respectively, **min** is to emphasise that the smallest of the mobilities is to be used and q is the absolute electronic charge. The rationale for preferring Eq. (7) is included in the following analysis, which we also use to establish whether the mobilities are hole or electron:

Whilst bimolecular recombination in organic semiconductors is known to follow the Langevin recombination (Mandoc et al. 2007; Koster et al. 2006; Blakesley et al. 2014; Koster et al. 2005; Deibel et al. 2008; Kirchartz) expression, which qualitatively proposes that the rate of recombination depends on the sum of the mobilities of both carriers (Braun 1984). Koster et al (2006) showed that this does not hold for polymer/fullerene bulk heterojunction solar cells. Ibid proposed that the Langevin recombination constant is dominated by the slowest charge carrier and its magnitude is given by Eq. (7). The rationale is that in BHJ polymer-fullerene, the electron (whose mobility is much greater than corresponding hole mobility) reaches the interface much earlier than the hole and the total time required for both carriers to reach the interface is determined by the hole, thus, carrier recombination is governed by the slower charge carrier. To accommodate the analysis, Koster et al. 2006 proposed Eq. (7), which is in contrast to Braun's proposal (Braun 1984) that $\gamma = \frac{q}{\varepsilon}\langle \mu_e + \mu_h \rangle$, where $\langle\ \rangle$ denotes the spatial average.

The proposal of slowest-only dominated Langevin recombination has also been authenticated by recent experiments (Koster et al. 2006) in which the recombination constant (1-*P*) γ (where *P* is the probability for dissociation (Mozer et al. 2005) of a bound electron–hole pair) has been measured directly in a polymer-fullerene [poly(2-methoxy-5-(2-ethylhexyloxy)-1,4-phenylenevinylene):PCBM] blend by Mozer et al. (2005) and

found to be 6×10^{-17} m^3s^{-1}, which gives $\gamma \approx 1.2 \times 10^{-16}$ m^3s^{-1}. Using $\mu_h = 2 \times 10^{-8}$ m^2/Vs (Melzer et al. 2004) and $P = 0.52$ (Koster et al. 2005), Koster et al. 2006 obtained $(1 - P)\gamma = 5.8 \times 10^{-17}$ m^3s^{-1}, which agreed with the experimental results by Mozer et al. 2005. The mobilities that we have determined in the present work lie in the low range category similar to those determined in Melzer et al.'s 2004. Hence we can conclude that our values in Table 2 must be hole mobilities and also the basis for our adoption of Eq. (7) in determining γ. SCLC conduction in polymer-fullerene blend devices is therefore limited by hole mobility. While the results show that the dark charge carrier mobility is very low, they also predict similar order and pattern of magnitude under illumination. This is mainly attributed to the structural disorder in the films (Shen et al. 2011) and the presence of trap states.

4.3 Effect of different active layer thicknesses on charge injection mechanisms at electrical contacts in the dark in ITO/PEDOT:PSS/P3HT:PCBM/Al devices

Although it currently appears difficult to establish a universal optimum active layer thickness (ALT) in excitonic devices, due to variations in polymer structure (regioregularity, molecular weight, poly-dispersity, etc.) and processing conditions (Thompson and Fréchet 2008), optimization of the active film thickness for given settings still remains crucial. Charge injection by electrodes could lead to the reduction of forward photocurrent due to electrode induced charge recombination. This is predominant especially in the accumulation of photogenerated minority charges in the vicinity of the electrodes as the injection of more opposite charges under illumination can lead to recombination losses.

In the present work, the charge injection processes at electrical contacts of the OPV devices constituting of varying active layers of thicknesses is studied. The variation in the thickness is suggested to determine the threshold open circuit voltage at the onset of quantum tunneling regime through variation of the transition voltage and the barrier height. To gain insight into the modifications and charge injection mechanisms, we analysed the J(V) data using the Fowler–Nordheim (FN) field- and the Richardson-Schottky (RS) thermionic- emission formalisms.

4.3.1 Fowler–Nordheim field emission analysis

Figure 6 shows the data of $\ln(J/V^2)$ vs (1/V) curves and the simulation curves using *F-N* tunneling model under reverse bias (RB) and forward bias (FB). In each of the devices, the reverse bias corresponds to electron injection through the ITO/PEDOT:PSS anode and to hole injection through the Al cathode. Forward bias ascribes to electron injection through the Al electrode and hole injection through the ITO/PEDOT:PSS electrode.

Under forward bias, $\ln\left(J/V^2\right)$ versus $(1/V)$ plots are linear with a negative slope at relatively high voltages (⇒ high electric fields) indicating that charge flow through the respective interfacial barriers is by quantum mechanical tunneling of predominantly holes. The slope of each of the linear fits in the tunneling regime is proportional to the corresponding barrier height. The presence of more than one slope, for example, *S*1 and *S*2 in the tunneling regime of the 61.5 nm *ALT*device indicates field dependence in barrier height. The nonlinear reverse bias *J–V* curves are indicative of field independent thermionic emission. The inflection point in each of the forward bias *FN* plots represents a transition from thermionic emission to field emission tunneling and this transition voltage v_{trans} varies with film thickness. The transition voltage values are highest for 77.1 and 84.5 nm film thickness. This shows that different potential barriers exist in the different devices.

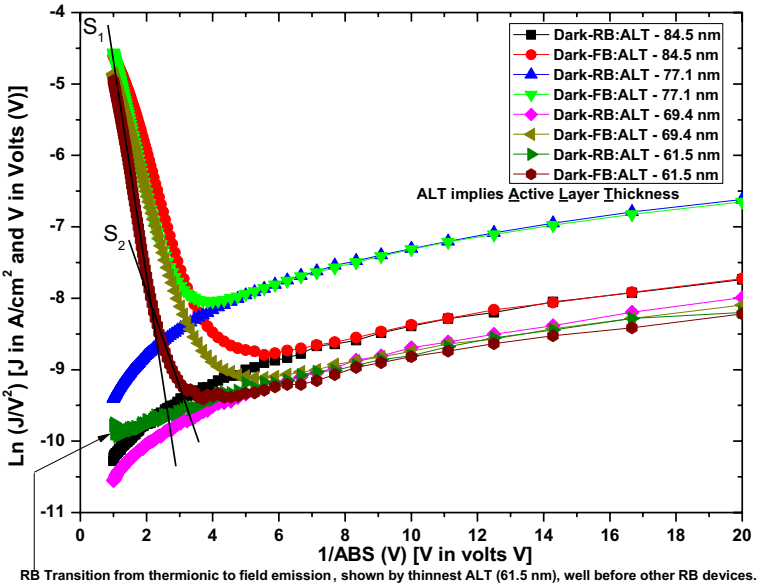

Fig. 6 Dark reverse bias (RB) and forward bias (FB) Fowler–Nordheim (FN) plots for ITO/PEDOT:PSS/P3HT:PCBM/Al devices with different active 1:1 P3HT:PCBM blend layer thicknesses

In the *FN* tunneling regime of Fig. 6, the slopes of the linear sections of the plots increase with decreasing active layer thicknesses. Also of interest is the 77.1 nm ALT device which exhibits the highest magnitude of the thermionic current density when compared with devices of other ALTs.

This adds onto other optimal characteristics already shown by the 77.1 nm ALT and it may indicate either the presence of the least pinhole (trap) density in this active layer or the prevalence of shallow traps.

Another peculiar characteristic is that at very high fields (~0.6 V) under *FB*, the curves tend to deviate from the FN straight lines. This behaviour is most likely caused by the very high increase in injected charge carriers (both electrons and holes, since the devices are double charge carriers) which outweigh what the bulk is able to transport and as a result builds up space charge that acts against more charge injection or the behaviour might be due to Poole Frenkel emission. We further note (in Fig. 6) that at very high electric fields, the curves coincide. This means that in this region, the current density is now independent of the different active layer thickness attributes. Under reverse bias (RB), it is only the 61.5 nm ALT device that shows onset of transition from thermionic emission to field emission and this occurs at a much higher field (~0.98 V applied voltage). Other thicknesses show neither onset of transition nor tunneling. This shows that RB barrier heights are much greater than those of their FB counterparts. Many competitive factors should be contributing to the resultant RB barrier heights.

4.3.2 Richardson-Schottky (RS) dark thermionic emission (TE) analysis

Figure 7 displays the dark J–V dependence of the studied devices having the differently thickened 1:1 P3HT:PCBM active layers.

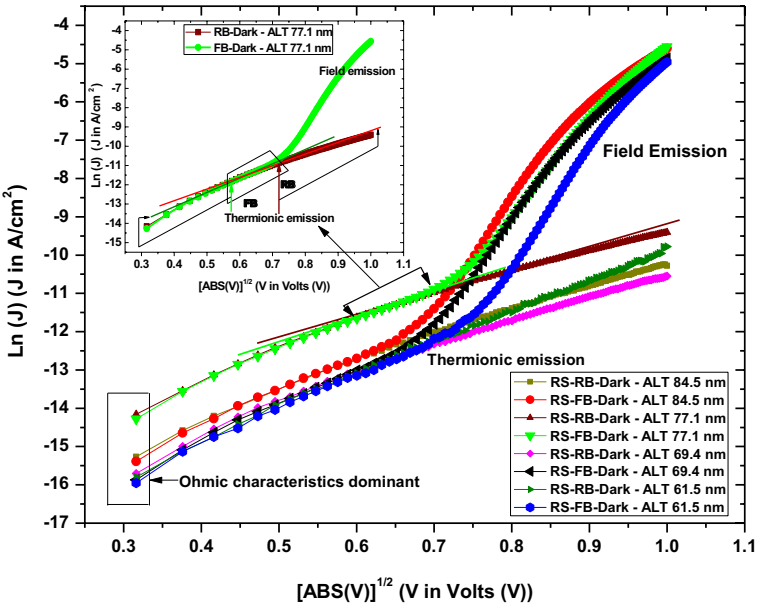

Fig. 7 Dark RS thermionic emission plots for ITO/PEDOT:PSS/P3HT:PCBM/Al devices with different active 1:1 P3HT:PCBM blend layer thicknesses under reverse bias (RB) and forward bias (FB)

The forward bias in Fig. 7 corresponds to electron injection into LUMO of PCBM from the negatively biased Al electrode and hole injection into HOMO of P3HT through ITO/PEDOT:PSS electrode. Reverse bias corresponds to electron injection into LUMO of P3HT and hole injection into HOMO of PCBM. Figure 8, illustrates forward and reverse biases associated with the optimal 77.1 nm ALT device. Straight lines in the RS plots indicate that charge flow through the interface is by thermionic emission and the nonlinear sections show that the injection of charge is by FN tunneling.

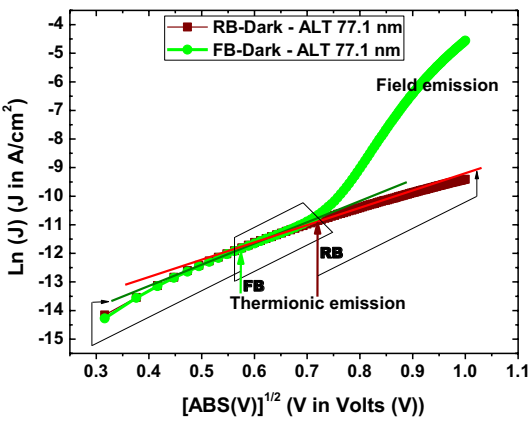

Fig. 8 Dark RS thermionic emission plot for the 77.1 nm 1:1 P3HT:PCBM blend ALT device under reverse and forward bias

5 Conclusion

The non-symmetric J–V curves and different rectification factors characteristic of the different active layer thickness devices confirm the existence of different and large potential energy barriers respectively, at the metal-active layer interfaces of the devices. Comparatively smaller barrier heights should be associated with the 77.1 nm ALT devices, which showed more prevalence of optimum J_{dark} values under forward and reverse biases in the identified electrical regions. No universal order of increase of current density with ALT for the different electrical regions of the polymer-fullerene based solar cells has been shown. Bulk heterojunction P3HT:PCBM solar cells exhibit very low charge carrier mobilities (μ values), which dependent upon electrical region. The highest (ohmic region) mobility is associated with the 77.1 nm active layer thick device and the lowest is ascribed to the 61.5 nm ALT, which is the thinnest. SCLC conduction in polymer-fullerene blend devices has been found to be limited by hole mobility. Charge carrier mobility was found to increase with increase in active film thickness up to the 77.1 nm ALT, which is also associated with optimal charge carrier mobility. Thereafter, the mobility decreased with increase in film thickness. Many competing mechanisms, like charge carrier dissociations and recombinations, account for bulk transport in BHJ P3HT:PCBM solar cells. In TFS-CLC region, bulk transport has been found to approximate Child's law.

Different potential barriers exist in different ALT devices. The tunneling regime potential barrier height φ increases as the thickness of the active layer decreases. At very high electric fields, the curves coincide. This means that in this region, the current density is now independent of the different active layer thickness attributes. RB barrier heights are much higher than those for FB. Whilst this study's empirical results demonstrated optimal performance at approximately 77.1 nm active layer thickness, the overall findings have demonstrated that the existence of a static universal optimum active layer thickness is not universal since such an optimum exhibits a contextual dependence.

Acknowledgements The authors would like to acknowledge the Material Physics Research Institute of the University of the Witwatersrand for research support and the incentive grant of the National Research Foundation for the financial support (UID 85675).

References

Apaydin, D.H., Yildiz, D.E., Cirpan, A., Toppare, L.: Optimizing the organic solar cell efficiency: the role of the active layer thickness. Sol. Energy Mater. Sol. Cells **113**, 100–105 (2013)

Bässler, H.: Charge transport in disordered organic photoconductors a Monte Carlo simulation study. Phys. Status Solidi B 175, 15–56 (1993)

Bartesaghi, D., Perez, I.D.C., Kniepert, J., Roland, S., Turbiez, M., Neher, D., Koster, J.A.: Nat. Commun. **6**, 7083–7090 (2015)

Blakesley, J.C., Castro, F.A., Kylberg, W., Dibb, G.F.A., Arantes, C., Valaski, R., Cremona, M., Kim, J.S., Kim, J.-S.: Towards reliable charge-mobility benchmark measurements for organic semiconductors. Org. Electron. **15**, 1263–1272 (2014)

Braun, L.: Electric field assisted dissociation of charge transfer states as a mechanism of photocarrier production. J. Chem. Phys. **80**, 4157–4161 (1984)

Braun, D.: Electronic injection and conduction processes for polymer devices. J. Polym. Sci. B **41**, 2622–2629 (2003)

Chiguvare, Z., 2005. Electrical and Optical Characterization of Bulk Heterojunction Polymer- Fullerene Solar Cells. Ph.D Thesis, Oldenburg University, Germany, 26.

Chirvase, D., Parisi, J., Hummelen, J.C., Dyakonov, V.: Influence of nanomorphology on the photovoltaic action of polymer-fullerene composites. Nanotechnology **15**(9), 1317–1323 (2004)
Das, R.R., Bhattacharya, P., Perez, W., Katiyar, R.S., Bhalla, A.S.: Leakage current characteristics of laser-ablated $SrBi_2Nb_2O_9$ thin films. Appl. Phys. Lett. **81**, 880–882 (2002)
Deibel, C., Wagenpfahl, A., Dyakonov, V.: Influence of charge carrier mobility on the performance of organic solar cells. Phys. Status Solidi RRL **2**, 175–177 (2008)
Dennler, G., Scharber, M.C., Ameri, T., Denk, P., Forberich, K., Waldauf, C., Brabec, C.J.: Design rules for donors in bulk-heterojunction tandem solar cells–towards 15% energy-conversion efficiency. Adv. Mater. **20**, 579–583 (2008)
Dimitrov, S.D., Schroeder, B.C., Nielsen, C.B., Bronstein, H., Fei, Z., McCulloch, I., Heeney, M., Durrant, J.R.: Singlet exciton lifetimes in conjugated films for organic solar cells. MDPI Polym. **8**, 1–12 (2016)
El-Nahass, M.M., Abd El-Rahman, K.F.: Nickel phthalocyanine thin films. J Alloys Compd. **430**, 194–199 (2007)
Gunduz, B., Yahia, I.S., Yakuphanoglu, F.: Electrical and photoconductivity properties of p-Si/P3HT/Al and p-Si/P3HT/MEH-PPV/Al organic devices: comparison study. Microelectron. Eng. **98**, 41–57 (2012)
Heiber, M.C., Okubo, T., Ko, S.-J., Luginbuhl, B.R., Ran, N.A., Wang, M., Wang, H., Uddin, M.A., Woo, H.Y., Bazan, G.C., Nguyen, T.-Q.: Measuring the competition between bimolecular charge recombination and charge transport in organic solar cells under operating conditions. Energy Environ. Sci. **11**, 3019–3031 (2018)
Henisch, H.K., 1984. Semiconductor Contacts, An approach to ideas and models. International Series of Monographs on Physics No.70. Clarendon Press, Oxford, vol. 70, p. 15.
https://one.laptop.org/
Huang, H.-L., Lee, C.-T., Lee, H.-Y.: Performance improvement mechanisms of P3HT: PCBM inverted polymer solar cells using extra PCBM and extra P3HT interfacial layers. Org. Electron. **21**, 126–131 (2015)
Islam, M.S., Islam, M.E., Bakar, A., Ismail, M., Baerwolff, H.: Influence of thickness and annealing temperature on the optical properties of spin-coated photoactive P3HT:PCBM blend. Opt. Photonics J. **3**, 28–32 (2013)
Kadem, B., Hassan, A., Cranton, W.: Efficient P3HT:PCBM bulk heterojunction organic solar cells; effect of post deposition thermal treatment. J. Mater Sci. Mater. Electron. **27**(7), 7038–7048 (2016)
Kadem, B.Y., Hassan, A.K., Cranton, W.: Enhancement of power conversion efficiency of P3HT:PCBM solar cell using solution processed Alq3 film as electron transport layer. J. Mater. Sci. Mater. Electron. **26**(6), 3976–3983 (2015)
Kandjani, S.A., Mirershadi, S., Nikniaz, A.: Inorganic-Organic Perovskite Solar Cells. Chpt. 8 224, 2015
Kao, K.C., Hwang, W.: Electrical Transport in Solids, with particular reference to organic semiconductors. Volume 14 of International Series in the Science of the Solid State. Pergamon Press, Oxford **14**, 418–422 (1981)
Kao, K.C., Hwang, W., Sang-I1, C., 1983. Electrical Transport in Solids. Pergamon, Oxford, Vol 36 (Issue 10), 90.
Kirchartz, T., Pieters, B., Taretto, K., Rau, U.: Mobility dependent efficiencies of organic bulk heterojunction solar cells: Surface recombination and charge transfer state distribution. Phys. Rev. B **80**, 035334 (2009)
Kirchartz, T., Agostinelli, T., Campoy-Quiles, M., Gong, W., Nelson, J.: Understanding the thickness-dependent performance of organic bulk heterojunction solar cells: influence of mobility, lifetime, and space charge. J. Phys. Chem. Lett. **3**, 3470–3475 (2012)
Koetse, M.M., Sweelssen, J., Hoekerd, K.T., Schoo, H.F.M., Veenstra, S.C., Kroon, J.M., Yang, X., Loos, J.: Efficient polymer:polymer bulk heterojunction solar cells. Appl. Phys. Lett. **88**, 083504 (2006)
Koster, L., Smits, E., Mihailetchi, V., Blom, P.: Device model for the operation of polymer/fullerene bulk heterojunction solar cells. Phys. Rev. B **72**, 085205 (2005)
Koster, L.J.A., Mihailetchi, V.D., Blom, P.W.M.: Bimolecular recombination in polymer/fullerene bulk heterojunction solar cells. Appl. Phys. Lett. **88**, 052104 (2006)
Krebs, F.C., Nielsen, T.D., Fyenbo, J., Wadstrøm, M., Pedersen, M.S.: Manufacture, integration and demonstration of polymer solar cells in a lamp for the "Lighting Africa" initiative. Energy Environ. Sci. **3**, 512–525 (2010)
Langevin, P.: Recombinaison et mobilites des ions dans les gaz. Ann. Chim. Phys. **28**, 287–433 (1903)
Liao, K.S., Yambem, S.D., Halder, A., Alley, N.J., Curran, S.A.: Designs and architectures for the next generation of organic solar cells. Energies **3**, 1212–1250 (2010)

Mandoc, M.M., Koster, L.J.A., Blom, P.: Optimum charge carrier mobility in organic solar cells. Appl. Phys. Lett. **90**, 133504–133507 (2007)
Melzer, C., Koop, E., Mihailetchi, V.D., Blom, P.W.M.: Hole transport in poly (phenylene vinylene)/methanofullerene bulk-heterojunction solar cells. Adv. Funct. Mater. **14**, 865–870 (2004)
Mesbahus, S., Arnab, S.M., Kabir, M.Z.: Analytical model for voltage-dependent photo and dark currents in bulk heterojunction organic solar cells. Academic Editor: Narottam Das **9**, 412 (2016)
Mozer, A.J., Sariciftci, N.S., Vanderzande, D., Österbacka, R., Westerling, M., Juška, G.: Charge transport and recombination in bulk heterojunction solar cells studied by the photoinduced charge extraction in linearly increasing voltage technique. Appl. Phys. Lett. **86**, 112104 (2005)
Nam, Y.M., Huh, J., Jo, W.H.: Optimization of thickness and morphology of active layer for high performance of bulk-heterojunction organic solar cells. Sol. Energy Mater. Sol. Cells **94**, 1118–1124 (2010)
Padinger, F., Rittberger, R.S., Sariciftci, N.S.: Effects of postproduction treatment on plastic solar cells. Adv. Funct. Mater. **13**(1), 85–88 (2003)
Peters, C.H., Sachs-Quintana, I.T., Kastrop, J.P., Beaupre, S., Leclerc, M., McGehee, M.D.: Adv. Energy Mater **1**(4), 491–494 (2011)
Qi, B., Wang, J.: Fill factor in organic solar cells. Phys. Chem. Chem. Phys. **15**, 8972–8982 (2013)
Scharber, M.C., Wuhlbacher, D., Koppe, M., Denk, P., Waldauf, C., Heeger, A.J., Brabec, C.L.: Design rules for donors in bulk-heterojunction solar cells–towards 10% energy-conversion efficiency. Adv. Mater **18**, 789–794 (2006)
Schilinsky, P., Waldauf, C., Brabec, C.J.: Recombination and loss analysis in polythiophene based bulk heterojunction photodetectors. Appl. Phys. Lett. **81**(20), 3885 (2002)
Servaites, J.D., Ratner, M.A., Marks, R.J.: Organic solar cells: a new look at traditional models. Energy Environ. Sci. **4**, 4410–4422 (2011)
Shaheen, S.E., Brabec, C.J., Sariciftci, N.S., Padinger, F., Fromherz, T., Hummelen, J.C.: 2.5% efficient organic plastic solar cells. Appl. Phys. Lett. **78**, 841–843 (2001)
Shen, Y., Li, K., Majumdar, N., Campbell, J.C., Gupta, M.C.: Bulk and contact resistance in P3HT:PCBM heterojunction solar cells. Sol. Energy Mater. Sol. Cells **95**, 2314–2317 (2011)
Shieh, J.-T., Liu, C.-H., Meng, H.-F., Tseng, S.-R., Chao, Y.-C., Horng, S.-F.: The effect of mobility in organic solar cells. J. Appl. Phys. **107**, 084503 (2010)
Sirringhaus, H., Brown, P.J., Friend, R.H., Nielsen, M.M., Bechgaard, K.: Two-dimensional charge transport in self-organized high-mobility conjugated polymers. Nature **401**(6754), 685–688 (1999)
Stevens, D.M., Qin, Y., Hillmyer, M.A., Frisbie, D.: Enhancement of the morphology and open circuit voltage in bilayer polymer/fullerene solar cells. J. Phys. Chem. C **113**, 11408–11415 (2009)
Sze, S.M.: Physics of Semiconductor Devices. Wiley, New York (1981)
Thompson, B.C., Fréchet, J.M.J.: Polymer-fullerene composite solar cells. Angew. Chem. Int. Ed. **47**, 58–77 (2008)
Wehenkel, D.J.: Physical processes in organic solar cells. Technische Universiteit Eindhoven, Eindhoven (2012)
Che, X., Li, Y., Qu, Y., Forrest, S. R.: High fabrication yield organic tandem photovoltaics combining vacuum- and solution-processed subcells with 15% efficiency. Nat. Energy. **3**, 422–427 (2018)

Affiliations

Lordwell Jhamba[1,2] · Daniel Wamwangi[1] · Zivayi Chiguvare[3]

[1] DST/Centre of Excellence in Strong Materials and Material Physics Research Institute, School of Physics, University of the Witwatersrand (Wits), Private Bag 3, Johannesburg 2050, South Africa

[2] Department of Physics, School of Mathematical and Natural Sciences, University of Venda, Private Bag X5050, Thohoyandou 0950, South Africa

[3] Department of Physics, University of Namibia, 340 Mandume Ndemufayo Ave, Pionierspark, Private Bag 13301, Windhoek, Namibia